




# High-performance all-solid-state Li–Se batteries induced by sulfide electrolytes†

Cite this: DOI: 10.1039/c8ee01621f

Received 5th June 2018,  
Accepted 18th July 2018

DOI: 10.1039/c8ee01621f

rsc.li/ees

Xiaona Li,‡ Jianwen Liang,‡ Xia Li, Changhong Wang, Jing Luo, Ruying Li and  
Xueliang Sun \*

All-solid-state Li–S batteries have attracted significant attention due to their high energy density and high safety. However, the insulating nature of S has limited the electrochemical performance of all-solid-state systems. Alternatively, Se, possessing orders of magnitude higher electronic conductivities, may be a promising cathode candidate but has been completely overlooked in all-solid-state battery systems. Herein, a feasible all-solid-state Li–Se battery is demonstrated using Se–Li<sub>3</sub>PS<sub>4</sub>–C as the cathode, Li<sub>3</sub>PS<sub>4</sub> as the electrolyte, and an Li–Sn alloy as the anode. In addition to the high electronic conductivity ( $1 \times 10^{-3} \text{ S cm}^{-1}$ ) of Se, a high Li<sup>+</sup> conductivity of  $1.4 \times 10^{-5} \text{ S cm}^{-1}$  across the Se–Li<sub>3</sub>PS<sub>4</sub> interface can be achieved. The all-solid-state Li–Se cell shows a high reversible capacity of 652 mA h g<sup>-1</sup> (96% of theoretical capacity) and exhibits favorable capacity retention upon cycling. This work demonstrates the advantages of a Se cathode in all-solid-state batteries and provides new opportunities for improving the charge transfer of S cathodes in solid-state batteries.

All-solid-state Li batteries using inorganic solid electrolytes are attracting intensive research attention due to their several distinctive advantages over state-of-the-art Li-ion batteries (LIBs).<sup>1–3</sup> Firstly, compared to flammable liquid electrolytes, the non-flammable nature of inorganic solid electrolytes can substantially improve battery safety and avoid electrolyte leakage. Secondly, the potential compatibility with Li metal anodes can enable high specific energy density, making them competitive candidates for mobile electronics, electric vehicles and large-scale energy storage systems. Conventional cathodes including LiCoO<sub>2</sub>,<sup>4</sup> LiMnO<sub>2</sub>,<sup>5</sup> LiNi<sub>0.5</sub>Mn<sub>1.5</sub>O<sub>4</sub>,<sup>6</sup> and LiFe<sub>0.2</sub>Mn<sub>0.8</sub>PO<sub>4</sub><sup>7</sup> have been investigated for all-solid-state LIBs. Moreover, the emergence of new battery chemistries and new opportunities for some electrodes that are comparable to liquid electrolytes has been witnessed.

Department of Mechanical and Materials Engineering, University of Western Ontario, 1151 Richmond St, London, Ontario, N6A 3K7, Canada.

E-mail: xsun9@uwo.ca

† Electronic supplementary information (ESI) available. See DOI: 10.1039/c8ee01621f

‡ These authors contributed equally to this work.

## Broader context

All-solid-state Li batteries using inorganic solid electrolytes have been regarded as advanced energy-storage systems due to their high safety and high energy density. However, these systems are still confronted with major challenges in terms of rechargeability, cycling stability and rate performance. The fatal weaknesses of all-solid-state Li batteries are poor Li<sup>+</sup> and electron transport between the electrode and the electrolyte. Although many sulfide-based solid-state electrolytes exhibit ultra-high Li<sup>+</sup> conductivities in bulk, the Li<sup>+</sup> transport through the interface still lags behind by several orders of magnitude. Therefore, developing new cathode materials with a compatible interface toward the electrolyte to achieve high interfacial Li<sup>+</sup> transport is one key strategy to realize high-performance all solid-state Li batteries. In this work, an all-solid-state Li–Se battery using the commercial Li<sub>3</sub>PS<sub>4</sub> electrolyte is proposed. Not only a high electronic conductivity of Se but also a high Li<sup>+</sup> conductivity across the Se–sulfide electrolyte interface is achieved. This work demonstrates an all-solid-state Li–Se battery as a promising high-energy storage system and provides new insights into solid-state electrode/electrolyte interfacial chemistry.

Since the 2000s, all-solid-state Li–S batteries have been studied as a promising alternative battery system due to their high theoretical energy densities (2567 W h kg<sup>-1</sup> compared to 387 W h kg<sup>-1</sup> for LIBs).<sup>8–11</sup> However, these systems are still confronted with major challenges in terms of rechargeability, cycling stability, coulombic efficiency and rate performance, which are far from commercialization. The fatal weaknesses of all-solid-state Li–S batteries are poor Li<sup>+</sup> and electron transport between the electrode and the electrolyte.<sup>10,12</sup> Unlike batteries with liquid electrolytes that can easily wet the electrodes and ensure smooth Li<sup>+</sup> transport, the Li<sup>+</sup> transport in solid-state batteries is highly limited at the electrode–electrolyte interface. Although many of the sulfide-based solid-state electrolytes exhibit high Li<sup>+</sup> conductivities ( $10^{-4}$  to  $10^{-2} \text{ S cm}^{-1}$  at room temperature<sup>13–17</sup>), the Li<sup>+</sup> transport through the interface can lag behind by several orders of magnitude.<sup>18,19</sup> For instance, the Li<sup>+</sup> conductivity of the Li–argyrodite phase Li<sub>6</sub>PS<sub>5</sub>Cl electrolyte is reported to be as high as  $1.3 \times 10^{-3} \text{ S cm}^{-1}$  in the bulk, but the conductivity is dramatically reduced to  $\sim 10^{-11} \text{ S cm}^{-1}$

at the interface with the  $\text{Li}_2\text{S}$  cathode.<sup>18</sup> In this context, the  $\text{Li}^+$  diffusion during electrochemical cycles is limited by the interfacial properties between the solid electrolyte and the active material rather than the bulk electrolyte. Meanwhile, the poor electronic conductivity of S cathodes is hindering the solid-state electrochemical reactions (lithiation/delithiation). In addition to engineering the S cathodes for all-solid-state batteries, developing new cathode materials with high ionic and electronic conductivities is another important approach to realize all-solid-state lithium batteries.

Compared to S, Se has much higher electronic conductivity ( $1 \times 10^{-3}$  vs.  $0.5 \times 10^{-27}$   $\text{S m}^{-1}$  at room temperature<sup>20–22</sup>). Herein, an all-solid-state Li–Se battery is developed for the first time. Although Se has been used as a cathode material in solid-state Ag-ion and Cu-ion batteries since 1968,<sup>23,24</sup> operating over a wide temperature range from room temperature to 150 °C, the corresponding working voltages are lower than 0.4 V. Different from previous reports, all-solid-state Li–Se battery chemistry with the commercial  $\text{Li}_3\text{PS}_4$  electrolyte was explored. The Li–Se battery exhibited a single discharge/charge plateau around 2.0 V ( $\text{Li}/\text{Li}^+$ ), corresponding to the typical conversion reaction between Se and  $\text{Li}_2\text{Se}$ . Significant improvements of both ionic and electronic conductivities of the cathode were achieved by ball-milling Se,  $\text{Li}_3\text{PS}_4$ , and acetylene black, ensuring fast and feasible charge transfer during electrochemical reaction processes. In particular, the  $\text{Li}^+$  transport over the Se– $\text{Li}_3\text{PS}_4$  interface is as high as  $1.4 \times 10^{-5}$   $\text{S cm}^{-1}$  after a ball-milling process. Compared with S, Se cathodes exhibit much lower polarization and higher reversibility at room temperature. After 100 discharge/charge cycles, the Se cathode retained a stable capacity of 585  $\text{mA h g}^{-1}$  and a retention of 90%.

Fig. 1a shows the scheme of an all-solid-state Li–Se battery based on Li or the Li–Sn alloy as the anode,  $\text{Li}_3\text{PS}_4$  as the electrolyte, and Se as the active material of the cathode. Typically, the Se

cathode was prepared by ball milling commercial Se,  $\text{Li}_3\text{PS}_4$ , and acetylene black (AB). Fig. 1b compares the initial discharge/charge curves between an all-solid-state Li–Se cell and a Li–S cell at 50  $\text{mA g}^{-1}$  at 25 °C. The Li–Se cell delivered an initial discharge capacity of 657  $\text{mA h g}^{-1}$  and a high coulombic efficiency of 98%. Although the Li–S cell showed a higher initial discharge capacity, the large irreversible capacity (310  $\text{mA h g}^{-1}$ , 37% of initial discharge capacity) limited its feasibility. The reversible charge capacity of the Li–Se cell (643  $\text{mA h g}^{-1}$ ) turned out to be substantially higher than that of the Li–S cell (527  $\text{mA h g}^{-1}$ ). Moreover, the Li–Se cell exhibited a significantly smaller polarization than that of the Li–S cell, indicating a higher energy efficiency and a more feasible electrochemical process of Se as compared to S. Basically, the much lower initial coulombic efficiency of the all-solid-state Li–S cell could be due to its large polarization, the intrinsically low ionic/electronic conductivity of  $\text{S}/\text{Li}_2\text{S}$ , and the fact that side reactions might be involved. The discharge and charge plateaus of Se were at about 2.0 and 2.3 V vs.  $\text{Li}/\text{Li}^+$ , and the polarization was only slightly higher than that of Se cathodes in conventional carbonate-based electrolytes.<sup>22</sup>

Galvanostatic intermittent titration technique (GITT) experiments were conducted at both 25 and 60 °C to determine the thermodynamic potential of the electrochemical reactions. The corresponding transient discharge/charge voltage profiles and the calculated polarization are shown in Fig. 1c and d, respectively. Similar to S cathodes in solid-state batteries,<sup>9</sup> the Se cathode presents only one plateau after full relaxation, which indicates a one-step solid–solid phase transition between  $\text{Li}_2\text{Se}$  and Se during the discharge/charge process. This is consistent with cyclic voltammogram (CV) measurements of the Se cathode (Fig. S1, ESI†). In addition, the polarization of the Se cathode remained very similar no matter whether at room temperature or 60 °C, exhibiting only a slight difference of 0.05 V over most of the capacity range. The reversible capacities were also almost unchanged. Evidently, the all-solid-state Li–Se cell demonstrated practical electrochemical performance at room temperature.

It is widely accepted that the charge transfer resistance, including both  $\text{Li}^+$  transportation and electron conduction resistance within the electrode composite, is a dominant factor restricting the electrochemical performance of all-solid-state batteries.<sup>12,25</sup> Unlike liquid electrolytes that can easily impregnate the porous electrodes, solid electrolyte particles show difficulty in providing seamless contact with the solid electrode materials even under high pressure. As a result, the  $\text{Li}^+$  conductivity across the electrode/electrolyte interface is usually orders of magnitude lower than that within the bulk electrolyte. While limited improvements for the electronic conductivity of electrodes could be achieved by incorporating electronic conductive additives *via* simple physical mixing, the successful utilization of an electronic conductive Se cathode can make a significant difference. To reveal the relatively faster reaction kinetics of the Se cathode over the S cathode in all-solid-state batteries, symmetric cells with configurations of  $\text{In}/\text{Se}-\text{Li}_3\text{PS}_4/\text{In}$  (molar ratio of Se-to- $\text{Li}_3\text{PS}_4$  similar to that of the  $\text{Se}-\text{Li}_3\text{PS}_4-\text{C}$  composite),  $\text{In}/\text{Li}_3\text{PS}_4/\text{In}$ , and  $\text{In}/\text{S}-\text{Li}_3\text{PS}_4/\text{In}$  were tested. The electrochemical impedance spectroscopy (EIS) measurements at different temperatures and the calculated conductivity results

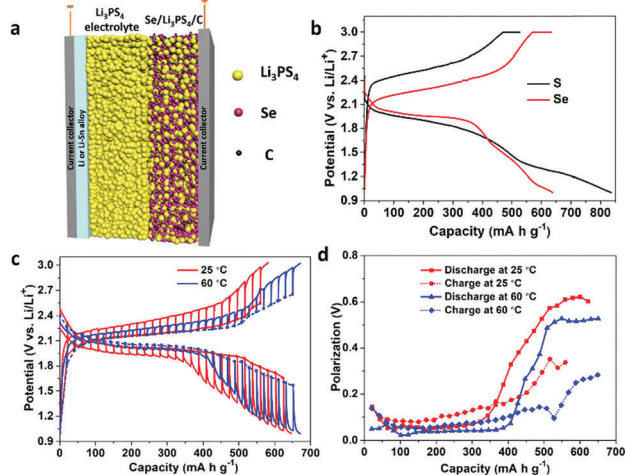


Fig. 1 (a) Schematic diagram of an all-solid-state Li–Se battery. (b) Typical discharge/charge profiles of Se and S cathodes in all-solid-state batteries at 50  $\text{mA g}^{-1}$  at room temperature. (c) Transient discharge/charge voltage profiles and (d) their corresponding polarization plots obtained by GITT for  $\text{Se}/\text{Li}_3\text{PS}_4/\text{Li}$  cells at room temperature and 60 °C.

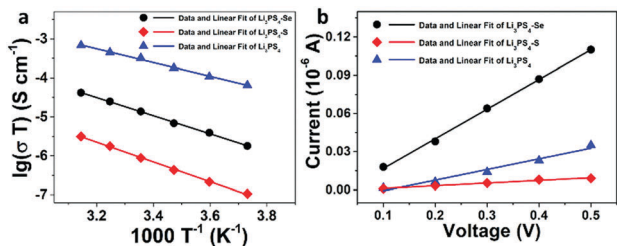


Fig. 2 (a) Temperature-dependent ionic conductivities of the commercial  $\text{Li}_3\text{PS}_4$ ,  $\text{Se-Li}_3\text{PS}_4$ , and  $\text{S-Li}_3\text{PS}_4$  after ball milling, and (b) equilibrium current of the commercial  $\text{Li}_3\text{PS}_4$ ,  $\text{Se-Li}_3\text{PS}_4$ , and  $\text{S-Li}_3\text{PS}_4$  after ball milling at different set voltages.

are compared in Fig. S2–S4 (ESI<sup>†</sup>) and Fig. 2a. Fitting the conductivities derived from the temperature dependent impedance using an Arrhenius law resulted in an activation energy of  $14.6 \text{ kJ mol}^{-1}$  and an ionic conductivity of  $3.0 \times 10^{-4} \text{ S cm}^{-1}$  for the commercial  $\text{Li}_3\text{PS}_4$  at room temperature, which is similar to the reported values.<sup>26,27</sup> Comparatively, the  $\text{Se-Li}_3\text{PS}_4$  composite delivered a similar room-temperature ionic conductivity of  $1.4 \times 10^{-5} \text{ S cm}^{-1}$ , and activation energy of  $19.3 \text{ kJ mol}^{-1}$ , whereas the ionic conductivity of the  $\text{S-Li}_3\text{PS}_4$  composite dramatically dropped to  $8.9 \times 10^{-7} \text{ S cm}^{-1}$ . The substantially higher ionic conductivity of the  $\text{Se-Li}_3\text{PS}_4$  composite than that of the  $\text{S-Li}_3\text{PS}_4$  composite counterpart, indicated a superior electrode–electrolyte interface of Se for  $\text{Li}^+$  migration.

Furthermore, the direct current (DC) electronic conductivities ( $\sigma_{\text{dc-electron}}$ ) of  $\text{Li}_3\text{PS}_4$ ,  $\text{Se-Li}_3\text{PS}_4$  and  $\text{S-Li}_3\text{PS}_4$  samples were measured using the symmetric cells. Fig. S5 (ESI<sup>†</sup>) shows the current evolution through time under different DC voltages ( $V_{\text{dc}}$  from 0.1 to 0.5 V) for the symmetric cells. At each  $V_{\text{dc}}$ , the current experienced a rapid decrease within a few seconds at the beginning and eventually reached equilibrium for all samples. The initial current decrease was related to the polarization and the equilibrium current ( $I_e$ ) was attributed to the electronic conductivity of the particular sample. As shown in the Fig. 2b and Fig. S5 (ESI<sup>†</sup>), the  $I_e$  of the  $\text{Se-Li}_3\text{PS}_4$  cell at 0.1 V was higher than the value of the  $\text{S-Li}_3\text{PS}_4$  and  $\text{Li}_3\text{PS}_4$  cells by about 150 and 6 times, respectively. Similar results observed at different voltages further prove the high electronic conductivity of  $\text{Se-Li}_3\text{PS}_4$ . The  $\sigma_{\text{dc-electron}}$  values of  $\text{Se-Li}_3\text{PS}_4$ ,  $\text{Li}_3\text{PS}_4$ , and  $\text{S-Li}_3\text{PS}_4$  were calculated to be  $3.0 \times 10^{-8}$ ,  $5.0 \times 10^{-9}$ , and  $2.0 \times 10^{-10} \text{ S cm}^{-1}$ , respectively, based on the DC method:<sup>28</sup>

$$\sigma_{\text{dc-electron}} = I_e L / (V_{\text{dc}} A)$$

where  $V_{\text{dc}}$  is the applied DC voltage;  $I_e$  is the equilibrium current after a certain period of time (10 min in this case);  $L$  is the thickness of the sample; and  $A$  is the electrode area.

Scanning electron microscopy (SEM) images and energy dispersive X-ray (EDX) mappings of the  $\text{Se-Li}_3\text{PS}_4\text{-C}$  cathode composite after ball milling confirm a homogenous distribution of the three components (Fig. S6–S8, ESI<sup>†</sup>). For the cross section view, cold-pressing results in relatively intimate contact between the cathodes and electrolytes as shown in Fig. 3a and b. For the electrochemical performance test, it was observed that the

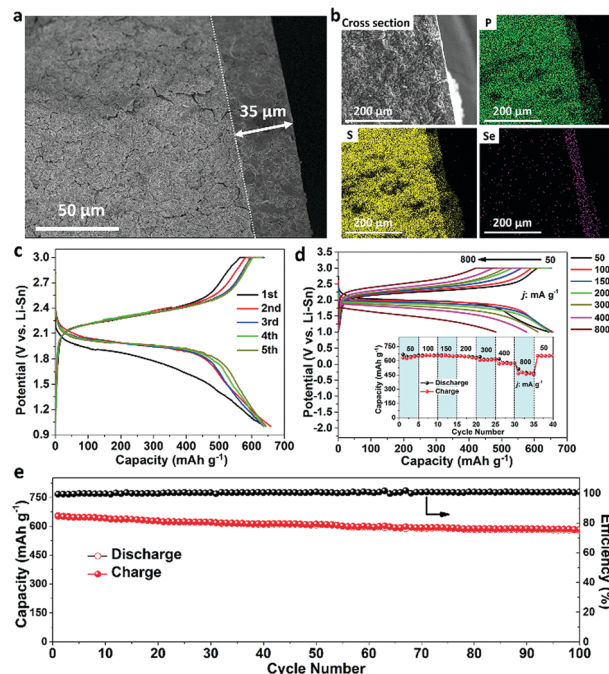


Fig. 3 (a) Cross-section SEM images of cathode/electrolyte pellets and (b) EDX mapping of Se, S and P elements. (c) Discharge/charge voltage profiles of the  $\text{Se/Li}_3\text{PS}_4/\text{Li-Sn}$  all-solid-state cell at  $50 \text{ mA g}^{-1}$ . (d) Representative discharge/charge voltage profiles at different current rates (inset: rate performance at current densities ranging from 50 to  $800 \text{ mA g}^{-1}$ ). (e) Cycling performance at  $50 \text{ mA g}^{-1}$  and corresponding coulombic efficiencies.

voltage changes abruptly during the charging process with bare Li as the anode (Fig. S9a, ESI<sup>†</sup>), and the voltage of the cell could not go up. Such a phenomenon should be due to internal short-circuit of the cell, which was found in another report using  $\text{Li}_2\text{S-P}_2\text{S}_5$  solid electrolyte.<sup>29</sup> Basically,  $\text{Li}_3\text{PS}_4$  is not electrochemically stable when it is in direct contact with bare Li during cycling,<sup>29,30</sup> and this was also proved by a sudden voltage drop in the symmetric  $\text{Li/Li}_3\text{PS}_4/\text{Li}$  cell (Fig. S9b, ESI<sup>†</sup>) after several plating/stripping processes. Thus, a Li–Sn alloy, which was obtained by melting commercial Li and Sn powder, was used as the anode to improve the stability of the anode/electrolyte interface.<sup>31</sup> The XRD pattern indicates the existence of both  $\text{Li}_{22}\text{Sn}_5$  and Li phases in the Li–Sn alloy (Fig. S10, ESI<sup>†</sup>), and the stable cycling performance of the Li–Sn/ $\text{Li}_3\text{PS}_4/\text{Li-Sn}$  symmetric cell (Fig. S11, ESI<sup>†</sup>) proved the enhanced stability of the anode/electrolyte interface.

The prototype all-solid-state  $\text{Se/Li}_3\text{PS}_4/\text{Li-Sn}$  cells were investigated for practicability at room temperature. As shown in the galvanostatic discharge/charge profiles in Fig. 3c, except for the first cycle, the  $\text{Se/Li}_3\text{PS}_4/\text{Li-Sn}$  cell retained a stable discharge plateau at approximately 2.0 V and a charge plateau at around 2.3 V at a current density of  $50 \text{ mA g}^{-1}$ . This prototype cell delivered a high reversible capacity of  $652 \text{ mA h g}^{-1}$  at  $50 \text{ mA g}^{-1}$ , achieving 96% of the theoretical capacity. Different from the conventional liquid cells with low initial coulombic efficiency, the  $\text{Se/Li}_3\text{PS}_4/\text{Li-Sn}$  cell exhibited a high coulombic efficiency of 97% in the first cycle, essentially minimizing irreversible side reactions.

A capacity of 585 mA h g<sup>-1</sup> and correspondingly a retention of 90% was retained after 100 cycles. The slight capacity decay might be attributed to the structural changes of the Se cathode as shown in SEM and EDX images of the cathode composites after 100 cycles (Fig. S12 and S13, ESI†). The rate performance of the Se/Li<sub>3</sub>PS<sub>4</sub>/Li–Sn cell was also tested, with reversible capacities of 652, 649, 642, 611, 574 and 462 mA h g<sup>-1</sup> at current densities of 100, 150, 200, 300, 400, and 800 mA g<sup>-1</sup>, respectively (Fig. 3d). When the current density was returned to 50 mA g<sup>-1</sup> after high rates, the capacity maintained a highly reversible capacity of 650 mA h g<sup>-1</sup>. The Se–Li<sub>3</sub>PS<sub>4</sub>–C electrode demonstrated good rate capability and essentially no sign of active material isolation within the cathode composites upon cycling.

Electrochemical impedance spectroscopy (EIS) measurements were performed at different discharge and charge states to monitor the internal resistance of the battery at 25 °C (Fig. S14, ESI†). Each EIS spectrum was fitted by the mode of L(CPE1-R1)(CPE2-R2)W, where the contributing parameters are defined as follows: R<sub>1</sub> at the high frequency represents the resistance of the solid electrolyte layer, and R<sub>2</sub> at the middle-frequency region suggests the interfacial charge transfer resistance between the solid electrolyte and the electrode. R<sub>1</sub> remains almost unchanged throughout the four different states, indicating the stable charge transfer of Li<sup>+</sup> in the bulk Li<sub>3</sub>PS<sub>4</sub> upon cycling. However, the increase in R<sub>2</sub> after cycling might be caused by the volume change of the cathode at different lithiation/delithiation states, which is possibly the reason for the slight capacity fading shown in Fig. 3e. Nevertheless, the impedance at different states tested over a 24 h period remained highly stable, indicating good compatibility of the electrochemical intermediates with the Li<sub>3</sub>PS<sub>4</sub> interlayer.

To investigate the mechanism of the Se cathode in the all-solid-state system, *in situ* Raman spectroscopy was performed as a powerful operando monitoring method (Fig. 4). Raman spectra of the Se/Li<sub>3</sub>PS<sub>4</sub>/C cathode, commercial Li<sub>3</sub>PS<sub>4</sub>, and pure Se are shown in Fig. S15 (ESI†). The pristine commercial Se displays two peaks at 139 and 233 cm<sup>-1</sup>, which should be attributed to E and A<sub>1</sub> modes of trigonal Se,<sup>32</sup> respectively. And for the spectrum of commercial Li<sub>3</sub>PS<sub>4</sub>, the main peak at 420 cm<sup>-1</sup> can be attributed to the PS<sub>4</sub><sup>3-</sup> structural unit.<sup>27,33</sup> For the Se/Li<sub>3</sub>PS<sub>4</sub>/C composites after a ball-milling process, three new peaks at 239, 252 and 352 cm<sup>-1</sup> were observed. The peak at 239 cm<sup>-1</sup> was attributed to Se with a slight blue-shift in

the Se/Li<sub>3</sub>PS<sub>4</sub>/C composites; the peak at 252 cm<sup>-1</sup> was associated with the symmetric bending of PS<sub>4-x</sub>Se<sub>x</sub><sup>3-</sup>,<sup>34–36</sup> and the weak peak at 352 cm<sup>-1</sup> could arise from the Se–S stretching vibrations based on previous reports.<sup>37,38</sup> Concluding from the Raman data, Se might interact with the Li<sub>3</sub>PS<sub>4</sub> solid electrolyte to form an interfacial species of PS<sub>4-x</sub>Se<sub>x</sub><sup>3-</sup> during the ball-milling process, and the EDX mapping of S and Se in Fig. 3b clearly confirms the overlap of S and Se within the cathode composite layer.

Fig. 4b and c depict the discharge/charge evolution of the Se and PS<sub>4-x</sub>Se<sub>x</sub><sup>3-</sup> species in the cathode composite by *in situ* Raman contour plots and spectra. During discharging, the peak at 239 cm<sup>-1</sup> gradually disappeared while the peak at 251 cm<sup>-1</sup> partially reduced, indicating different extents of lithiation for the Se<sub>n</sub> chains and the PS<sub>4-x</sub>Se<sub>x</sub><sup>3-</sup> species. Complete lithiation of Se and mild lithiation of the PS<sub>4-x</sub>Se<sub>x</sub><sup>3-</sup> species can be reasonably inferred. During charging, both peaks gradually retrieved the initial intensities before discharging. Evidently, the lithiation/delithiation processes of the two species were highly reversible. Furthermore, the peak assigned to the Se–S stretching vibration at around 352 cm<sup>-1</sup> could be observed during the entire discharge/charge process, with a trace of reversible change. This electrochemical mechanism is different from the liquid electrolyte based reactions and is unique to the all-solid-state system. The reversible lithiation/delithiation reactions of the interfacial species are reported for the first time.

X-ray photoelectron spectroscopy (XPS) analysis of the Se cathode at different discharge/charge states was intended to reveal the surface chemistry of the cathode. It was found that the XPS spectra of Se overlap severely with the other three elements in the cathode composites (Se 3d overlapped with Li 1s, Se 3p overlapped with S 2p, and Se LLMb Auger overlapped with P 2p), which makes it particularly difficult to differentiate the exact species. While obvious reduction/oxidation of Se could still be seen from the fitted Li 1s and Se 3d XPS spectra (Fig. S16, ESI†), the Se 3d<sub>5/2</sub> spectra shifted to lower binding energy (54.8 eV to 52.4 eV) and then recover back to the pristine state after full charge to 3.0 V. *Ex situ* XRD results shown in Fig. S17 (ESI†) further confirm the conversion of Se into Li<sub>2</sub>Se at the discharge state and recovery of Se at the full charge state.

## Conclusions

In conclusion, we successfully demonstrated feasible all-solid-state Li–Se batteries with good electrochemical performance for the first time. The Se cathode composite exhibited significantly higher utilization and lower polarization compared to S in the all-solid-state battery system at room temperature. Impedance and DC electronic conductivity tests of the In/Se–Li<sub>3</sub>PS<sub>4</sub>/In and In/S–Li<sub>3</sub>PS<sub>4</sub>/In symmetric cells proved the superior ionic and electronic conductivities of the Se–Li<sub>3</sub>PS<sub>4</sub> component as compared to S–Li<sub>3</sub>PS<sub>4</sub>. Fast charge transfer was likewise achieved in the Se–Li<sub>3</sub>PS<sub>4</sub>–C cathode. The conversion of Se into Li<sub>2</sub>Se at the discharged state and the recovery of Se at the fully charged state were observed *via ex situ* XRD. Moreover, the *in situ* Raman

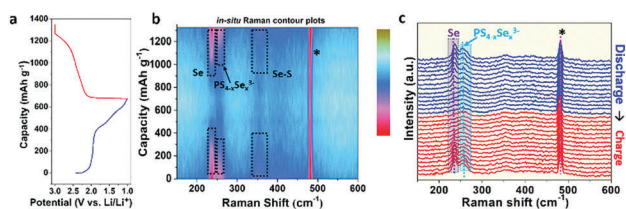


Fig. 4 Characterizations of the Se cathode during the first cycle: (a) discharge/charge profile, (b) capacity dependent *in situ* Raman spectral contour plots, and (c) *in situ* Raman spectra at different discharge/charge states. The signal marked as “\*” in the spectra should be caused by the fluorescent lamp during test.

analysis not only revealed the detailed evolution of the Se cathode during the discharge/charge process, but also provided evidence for the unique lithiation/delithiation reactions of the reversible interfacial  $\text{PS}_{4-x}\text{Se}_x^{3-}$  species (formed after a ball-milling process) in the cathode composite. This work demonstrates all-solid-state Li-Se batteries as a promising high-energy storage system and provides new insights on solid-state electrode/electrolyte interfacial chemistry. Compositing Se and S for an advanced hybrid cathode could be a new strategy for enabling high-performance all-solid-state Li batteries. Fine tuning the balance between the ionic and electronic conductive Se and the high capacity S is currently under investigation.

## Conflicts of interest

There are no conflicts to declare.

## Acknowledgements

This work was supported by the Natural Sciences and Engineering Research Council of Canada (NSERC), Canada Research Chair Program (CRC), China Automotive Battery Research Institute, Canada Foundation for Innovation (CFI), and University of Western Ontario.

## References

- 1 A. Manthiram, X. Yu and S. Wang, *Nat. Rev. Mater.*, 2017, **2**, 16103.
- 2 C. Sun, J. Liu, Y. Gong, D. P. Wilkinson and J. Zhang, *Nano Energy*, 2017, **33**, 363–386.
- 3 R. Xu, S. Zhang, X. Wang, Y. Xia, X. Xia, J. Wu, C. Gu and J. Tu, *Chem. – Eur. J.*, 2017, **23**, 13950–13956.
- 4 N. Ohta, K. Takada, I. Sakaguchi, L. Zhang, R. Ma, K. Fukuda, M. Osada and T. Sasaki, *Electrochem. Commun.*, 2007, **9**, 1486–1490.
- 5 J. Auvergniot, A. Cassel, J.-B. Ledeuil, V. Viallet, V. Seznec and R. Dedryvère, *Chem. Mater.*, 2017, **29**, 3883–3890.
- 6 G. Oh, M. Hirayama, O. Kwon, K. Suzuki and R. Kanno, *Chem. Mater.*, 2016, **28**, 2634–2640.
- 7 J. Ju, Y. Wang, B. Chen, J. Ma, S. Dong, J. Chai, H. Qu, L. Cui, X. Wu and G. Cui, *ACS Appl. Mater. Interfaces*, 2018, **10**, 13588–13597.
- 8 T. Kobayashi, Y. Imade, D. Shishihara, K. Homma, M. Nagao, R. Watanabe, T. Yokoi, A. Yamada, R. Kanno and T. Tatsumi, *J. Power Sources*, 2008, **182**, 621–625.
- 9 X. Yao, N. Huang, F. Han, Q. Zhang, H. Wan, J. P. Mwizerwa, C. Wang and X. Xu, *Adv. Energy Mater.*, 2017, **7**, 1602923.
- 10 Z. Lin, Z. Liu, N. J. Dudney and C. Liang, *ACS Nano*, 2013, **7**, 2829–2833.
- 11 H. Qu, J. Zhang, A. Du, B. Chen, J. Chai, N. Xue, L. Wang, L. Qiao, C. Wang, X. Zang, J. Yang, X. Wang and G. Cui, *Adv. Sci.*, 2018, **5**, 1700503.
- 12 F. Han, J. Yue, X. Fan, T. Gao, C. Luo, Z. Ma, L. Suo and C. Wang, *Nano Lett.*, 2016, **16**, 4521–4527.
- 13 Y. Kato, S. Hori, T. Saito, K. Suzuki, M. Hirayama, A. Mitsui, M. Yonemura, H. Iba and R. Kanno, *Nat. Energy*, 2016, **1**, 16030.
- 14 N. Kamaya, K. Homma, Y. Yamakawa, M. Hirayama, R. Kanno, M. Yonemura, T. Kamiyama, Y. Kato, S. Hama and K. Kawamoto, *Nat. Mater.*, 2011, **10**, 682.
- 15 H. J. Deiseroth, S. T. Kong, H. Eckert, J. Vannahme, C. Reiner, T. Zaiss and M. Schlosser, *Angew. Chem., Int. Ed.*, 2008, **47**, 755–758.
- 16 Z. Liu, W. Fu, E. A. Payzant, X. Yu, Z. Wu, N. J. Dudney, J. Kiggans, K. Hong, A. J. Rondinone and C. Liang, *J. Am. Chem. Soc.*, 2013, **135**, 975–978.
- 17 Y. Seino, T. Ota, K. Takada, A. Hayashi and M. Tatsumisago, *Energy Environ. Sci.*, 2014, **7**, 627–631.
- 18 C. Yu, S. Ganapathy, N. J. de Klerk, I. Roslon, E. R. van Eck, A. P. Kentgens and M. Wagemaker, *J. Am. Chem. Soc.*, 2016, **138**, 11192–11201.
- 19 C. Yu, S. Ganapathy, E. R. Van Eck, H. Wang, S. Basak, Z. Li and M. Wagemaker, *Nat. Commun.*, 2017, **8**, 1086.
- 20 A. Eftekhari, *Sustainable Energy Fuels*, 2017, **1**, 14–29.
- 21 J. Xu, J. Ma, Q. Fan, S. Guo and S. Dou, *Adv. Mater.*, 2017, **29**, 1606454.
- 22 C. P. Yang, S. Xin, Y. X. Yin, H. Ye, J. Zhang and Y. G. Guo, *Angew. Chem., Int. Ed.*, 2013, **52**, 8363–8367.
- 23 T. Takahashi and O. Yamamoto, *J. Appl. Electrochem.*, 1977, **7**, 37–43.
- 24 T. Takahashi and O. Yamamoto, *J. Electrochem. Soc.*, 1970, **117**, 1–5.
- 25 J. M. Whiteley, S. Hafner, S. S. Han, S. C. Kim, K. H. Oh and S. H. Lee, *Adv. Energy Mater.*, 2016, **6**, 1600495.
- 26 K. Homma, M. Yonemura, T. Kobayashi, M. Nagao, M. Hirayama and R. Kanno, *Solid State Ionics*, 2011, **182**, 53–58.
- 27 N. H. H. Phuc, K. Morikawa, M. Totani, H. Muto and A. Matsuda, *Solid State Ionics*, 2016, **285**, 2–5.
- 28 H. Morimoto, H. Yamashita, M. Tatsumisago and T. Minami, *J. Am. Ceram. Soc.*, 1999, **82**, 1352–1354.
- 29 M. Nagao, A. Hayashi and M. Tatsumisago, *Electrochem. Commun.*, 2012, **22**, 177–180.
- 30 F. Han, J. Yue, X. Zhu and C. Wang, *Adv. Energy Mater.*, 2018, **8**, 1703644.
- 31 X. Fan, J. Yue, F. Han, J. Chen, T. Deng, X. Zhou, S. Hou and C. Wang, *ACS Nano*, 2018, **12**, 3360–3368.
- 32 M. Gorman and S. A. Solin, *Solid State Commun.*, 1976, **18**, 1401–1404.
- 33 T. Hakari, M. Deguchi, K. Mitsuhashi, T. Ohta, K. Saito, Y. Orikasa, Y. Uchimoto, Y. Kowada, A. Hayashi and M. Tatsumisago, *Chem. Mater.*, 2017, **29**, 4768–4774.
- 34 J. Kim, Y. Yoon, M. Eom and D. Shin, *Solid State Ionics*, 2012, **225**, 626–630.
- 35 K. Yang, J. Dong, L. Zhang, Y. Li and L. Wang, *J. Am. Ceram. Soc.*, 2015, **98**, 3831–3835.
- 36 L. Zhang, K. Yang, J. Mi, L. Lu, L. Zhao, L. Wang, Y. Li and H. Zeng, *Adv. Energy Mater.*, 2015, **5**, 1501294.
- 37 H. Eysel and S. Sunder, *Inorg. Chem.*, 1979, **18**, 2626–2627.
- 38 X. Li, J. Liang, K. Zhang, Z. Hou, W. Zhang, Y. Zhu and Y. Qian, *Energy Environ. Sci.*, 2015, **8**, 3181–3186.